Eur. Phys. J. B (2016) 89: 58
DOI: 10.1140/epjb/e2016-60932-x

THE EUROPEAN PHYSICAL JOURNAL B

Regular Article

Defective graphene and nanoribbons: electronic, magnetic and structural properties

Thiago Guerra[1], Sérgio Azevedo[1,a], and Marcelo Machado[2]

[1] Departamento de Física/CCEN, Universidade Federal da Paraíba Caixa Postal 5008, 58051-900 João Pessoa-PB, Brazil
[2] Departamento de Física, Universidade Federal de Pelotas Caixa Postal 354, 96010-900 Pelotas-RS, Brazil

Received 1st December 2015 / Received in final form 18 January 2016
Published online 2 March 2016 –

Abstract. We make use of first-principles calculations, based on the density functional theory (DFT), to investigate the alterations at the structural, energetic, electronic and magnetic properties of graphene and zigzag graphene nanoribbons (ZGNRs) due to the inclusion of different types of line and punctual defects. For the graphene it is found that the inclusion of defects breaks the translational symmetry of the crystal with drastic changes at its electronic structure, going from semimetallic to semiconductor and metallic. Regarding the magnetic properties, no magnetization is observed for the defective graphene. We also show that the inclusion of defects at ZGNRs is a good way to create and control pronounced peaks at the Fermi level. Furthermore, defective ZGNRs structures show magnetic moment by supercell up to $2.0\mu_B$. For the non defective ZGNRs is observed a switch of the magnetic coupling between opposite ribbon edges from the antiferromagnetic to the ferrimagnetic and ferromagnetic configurations.

1 Introduction

Graphene is a monolayer of carbon (C) atoms presenting sp^2 hybridization and arranged in a one atom thick two-dimensional hexagonal honeycomb structure [1]. This material has attracted the scientific interest due to the challenges related to the complete understanding of its properties as well as the rich physics involved in its description. Graphene is the most resistant material ever measured, being flexible, absorbing 2.3% of white light and presenting high electronic mobility at room temperature [2–4]. It possesses an interesting electronic structure, being a semimetal (zero gap semiconductor) with zero energy gap and having a null density of states (DOS) at the Fermi level (E_f) [5]. Due to a linear electronic dispersion relation, the charge carriers in graphene mimic relativistic particles with zero rest mass which can be described by the Dirac relativistic equation. Furthermore, graphene can be seen as the fundamental building block when constructing C nanostructures such as the zero-dimensional fullerenes, one-dimensional nanotubes (NTs) and nanoribbons (NRs), and three-dimensional graphite [6], being synthesized through different techniques [7–9].

Graphene nanoribbons (GNRs) can be generated by cutting graphene sheets off. Depending on the way the cut is performed the GNRs can present different forms, edge types known as armchair (AGNRs) or zigzag (ZGNRs), and widths [10]. Exotic electronic and magnetic properties can arise when we cut graphene into GNRs. For example, we can have size, edge type, and width dependent adjustable energy gaps [11]; edge special states [12]; ferromagnetic (FM) or antiferromagnetic (AFM) states at both edges or FM at one edge and AFM at the other, depending on the ribbon width and the presence of an external electric field [13]; electronic structure intimately related with the magnetic interaction between edges [14]; ballistic transport of charge [15]. These remarkably electronic and magnetic properties would make the GNRs good candidates to be used as active parts of nanoelectronics and spintronics devices, if they could be custom-made synthesized. Actually, GNRs can be obtained through several experimental techniques such as lithography [16,17], using molecular precursors and linear polymers [18,19], unzipping multiwalled nanotubes [20], and epitaxially grown on silicon carbide [15]. However, most of the proposed applications require the ability to adjust the wanted properties at nanoscale, and several theoretical and experimental methods were proposed in order to do that [14,21–25].

Another possible way to alter the GNRs properties is to incorporate line defects (LDs) at their perfect hexagonal lattice [26–29]. Defects, which are inevitably created during the GNRs growth process, can be used to tune the GNRs electronic and magnetic properties, offering new possibilities when one thinks about applications. Recently, Chen et al. [29] have synthesized a line defect composed by two pairs of pentagonal rings surrounding one octagonal ring (558-LD) replacing the hexagons in a graphene sheet. In another work, Li et al. [30] have proposed a way

[a] e-mail: sazevedo@fisica.ufpb.br

to generate one stable line defect at graphene, formed by tetragonal carbon rings (4-LD). A similar type of line defect was observed at a MoS_2 sheet [31]. Botello-Méndez and collaborators showed that different divacancy defects could be formed in graphene [32]. Removing carbon dimers oriented perpendicularly to the zigzag chains we can obtain a LD composed by tetradecanal carbon rings (14-LD). Also, Ugeda and co-workers have shown that divacancies at a graphene sheet can generate a punctual defect (PD) formed by two pentagonal rings reconstructed and separated by one octagonal ring (585-PD) [33]. Finally, Liu and colleagues have shown that a line defect containing one tetragonal and one octagonal ring (48-LD) can be formed by dislocations at a boron nitride sheet [34]. At this context, in this paper we investigate, using first-principles calculations, how the 558-, 4-, 14-, and 48-LD and 585-PD influence the graphene and ZGNRs electronic properties. Also, we investigate the energetic cost to the formation of such defects and their influence at the magnetic properties of ZGNRs.

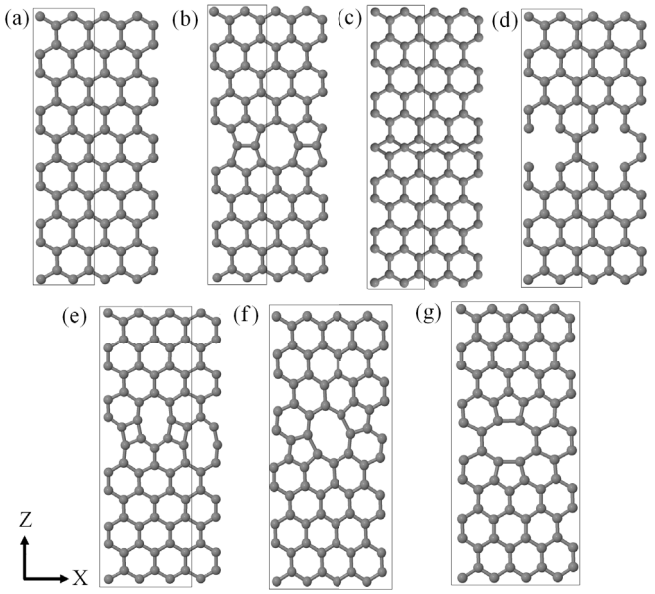

Fig. 1. Pictorial scheme for the studied graphene sheets after optimization: (a) Pristine and presenting a line defect composed by: (b) two pentagonal and one octagonal ring (558-LD), (c) tetragonal rings (4-LD), (d) tetradecanal rings (14-LD), (e) one tetragonal and one octagonal ring (48-LD). At (f) and (g) we have the punctual defects composed by two pentagons separated by one octagon in two different arrangements (585-PD_1 and 585-PD_2, respectively). The supercell of each graphene sheet is shown inside the boxes and the carbon atoms are represented by the gray spheres.

2 Methodology

2.1 Modeling

The calculations were performed using the Spanish Initiative for Electronic Simulations with Thousands of Atoms (SIESTA) code [35,36]. It is used for predicts physical properties as electronic structure, spin polarization, energies, atomic forces, geometry optimization, local density of states, density of state, charge and spin of atoms, molecule and solids. It was utilized in this study to investigate how the electronic, structural, energetic and magnetic properties for graphene and ZGNRs are changed by the inclusion of line and punctual defects. SIESTA performs full self-consistent calculations within the density functional theory (DFT) [37] solving the Kohn-Sham equation for the electrons using a basis set of numerical atomic orbitals in the generalized gradient approximation (GGA) [38] with the exchange and correlation terms parametrized for Perdew-Burke-Ernzerhof [39]. The interactions between electrons and core are described by non-local norm-conserving Troullier-Martins pseudopotential [40] factorized in the Kleinman-Bylander form [41] and a double-ζ basis-set composed by numeric atomic orbitals with a cut-off radius of ≈15.0 Å. In the calculations, only the valence orbitals were treated self-consistently, namely we consider $1s$ for H and $2s2p$ for C. The pseudopotentials were generated with these atomic valence-electron configurations. All of the geometries were optimized using the conjugate gradient method until the residual Hellmann-Feynman forces acting on any atom were smaller than 0.1 eV/Å. We adopt a rectangular supercell where the graphene and ZGNRs have different sizes and numbers of atoms for each type of defect. The calculations were performed at absolute zero and in vacuum.

The seven studied graphene system supercells, after optimization, can be seen at Figure 1. At Figure 1a we have a pristine graphene sheet, while at Figure 1b we can observe a line defect, at the middle of the sheet, formed by the alternation of pentagon pairs and octagons (558-LD). At Figure 1c we have a graphene sheet with a line defect composed by distorted tetragonal rings (4-LD). These structures can be obtained from two graphene sheets dislocated towards each other together with the remotion of some atoms and posterior reconstruction of the sheet containing a LD [30]. At Figure 1d we can see a line defect, in the middle of the sheet, which is formed by tetradecanal rings (14-LD). This type of system can be formed by the presence of a line of divacancies. At Figure 1e we have a LD formed by one tetragonal and one octagonal rings (48-LD) which can be obtained through dislocations [34]. Figure 1f shows a graphene layer with a punctual defect composed by two pentagonal rings separated by one octagon and no dangling bonds (585-PD_1), type of defect formed by a divacancy [33]. Finally, at Figure 1g we have the 585-PD_2, which is similar to the previous one with the octagonal ring rotated or the creation of divacancies on different lattice points in the lattice. Together with the graphene study, we have also investigated how the same defects affect the zigzag nanoribbons properties. The studied ZGNRs present the same configuration shown by the graphene sheets, being saturated along the X direction (see Fig. 2), which is the growth direction for the ribbons. For the graphene layers, the systems are grown along the X and Z directions.

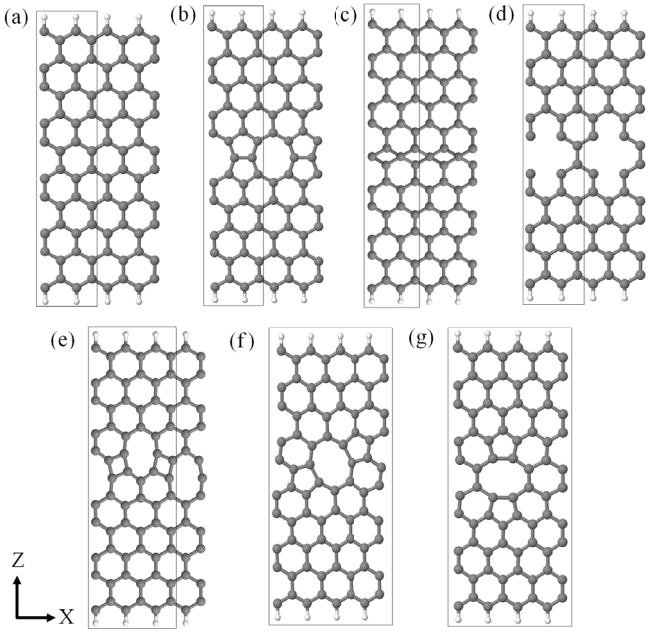

Fig. 2. Pictorial scheme for the studied zigzag graphene nanoribbons after optimization: (a) Pristine 10-ZGNR and presenting a line defect composed by: (b) two pentagonal and one octagonal ring (558-LD-ZGNR), (c) tetragonal rings (4-LD-ZGNR), (d) tetradecanal rings (14-LD-ZGNR), (e) one tetragonal and one octagonal ring (48-LD-ZGNR). At (f) and (g) we have the punctual defects composed by two pentagons separated by one octagon in two different arrangements (585-PD_1-ZGNR and 585-PD_2-ZGNR, respectively). The supercell of each ZGNR is shown inside the boxes and the carbon (hydrogen) atoms are represented by the gray (white) spheres.

2.2 Stability

To perform this analysis we make use of the zero temperature thermodynamic approach based on the chemical potential determination as described in previous works [42,43]. In this approach, the formation energy by atom (E_{for}) can be written as:

$$E_{\text{for}} = \frac{E_{\text{tot}} - n_{\text{CC}}\mu_{\text{CC}} - n_{\text{HC}}\mu_{\text{HC}}}{n_t}, \quad (1)$$

where E_{tot} is the calculated system total energy, n_{CC} and n_{HC} are the number of C and H atoms, respectively, μ_{CC} and μ_{HC} are the chemical potentials calculated for C-C and H-C bonds, respectively, and $n_t = n_{\text{CC}} + n_{\text{HC}}$ is the total number of atoms.

The chemical potential for C-C bonds is obtained through a total energy calculation for an infinite graphene monolayer ($E_{\text{tot}}^{\text{layer}}$). Therefore, we have:

$$\mu_{\text{CC}} = \frac{E_{\text{tot}}^{\text{layer}}}{n_{\text{CC}}} = -154.86 \text{ eV/atom}. \quad (2)$$

We have used H atoms to saturate the edge dangling bonds. Taking this into account, we have calculated the chemical potential for the H-C bonds (μ_{H}) using the total energy calculation from a finite C layer ($E_{\text{tot}}^{\text{layer}}$) saturated with H atoms, we have:

$$\mu_{\text{HC}} = \frac{E_{\text{tot}}^{\text{layer}} - n_{\text{CC}}\mu_{\text{CC}}}{n_{\text{HC}}} = -15.71 \text{ eV/atom}. \quad (3)$$

Using these values for the chemical potentials and knowing n_{CC}, n_{HC}, and having the total energy value calculated for each system, the E_{for} can be calculated via equation (1).

3 Results and discussion

3.1 Graphene

3.1.1 Electronic properties

Here we analyse the alterations at the electronic properties of graphene layers due to the inclusion of defects as shown at Figure 1. At Figure 3 we have the band structures for these graphene systems.

At Figure 3a we have the characteristic band structure of graphene (pristine), in which there is a single point crossing (Dirac point) of valence and conduction bands and a null DOS at the Fermi level (as can be seen at Fig. 4a). By inserting one unidimensional topological defect, composed by two pentagonal and one octagonal sp^2 hybridized rings (558-LD), although the system maintains its semi-metallic character, we change its electronic configuration with the states, which presented a linear dispersion close to the X point at Fermi level, becoming flatter (Fig. 3b). Also, the Dirac cone is considerably reduced and we can observe the presence of a state, which was degenerated before, crossing it at the valence band together with a state split at the conduction band. On the other hand, similar to what happens for the pristine system, we have a null DOS with two peaks next to the Fermi level region as can be seen at Figure 4b. In a previous work, Lahiri and collaborators showed that the 558-LD acts as a quasi-one-dimensional metallic wire with one state at the Fermi level and a respective peak at the DOS [28]. In our case, two states are observed near the Fermi level resulting in two peaks at this region. In another work, Chen and colleagues showed a significant suppression at the conductance at the Dirac point due to the line defect inclusion [29]. This effect can be associated with the states splitting at the conduction band. The incorporation, at the graphene, of a LD containing tetragonal carbon rings (4-LD), with the middle carbon atoms of the LD presenting a sp^3-like hybridization and having the valence electrons saturated, causes no drastic changes at the electronic structure of graphene. As can be seen at Figure 3c, this type of defect maintains the Dirac point and its semi-metallic properties, also introducing two states on both sides of the Fermi level. As a consequence, we have two large peaks at the DOS in this region as can be seen at Figure 4c. The removal of carbon dimers, oriented perpendicularly to the zigzag chains, introduces a 14-LD in the graphene sheet resulting in two lines of sp^2 hybridized carbon atoms having σ dangling bonds. The presence of

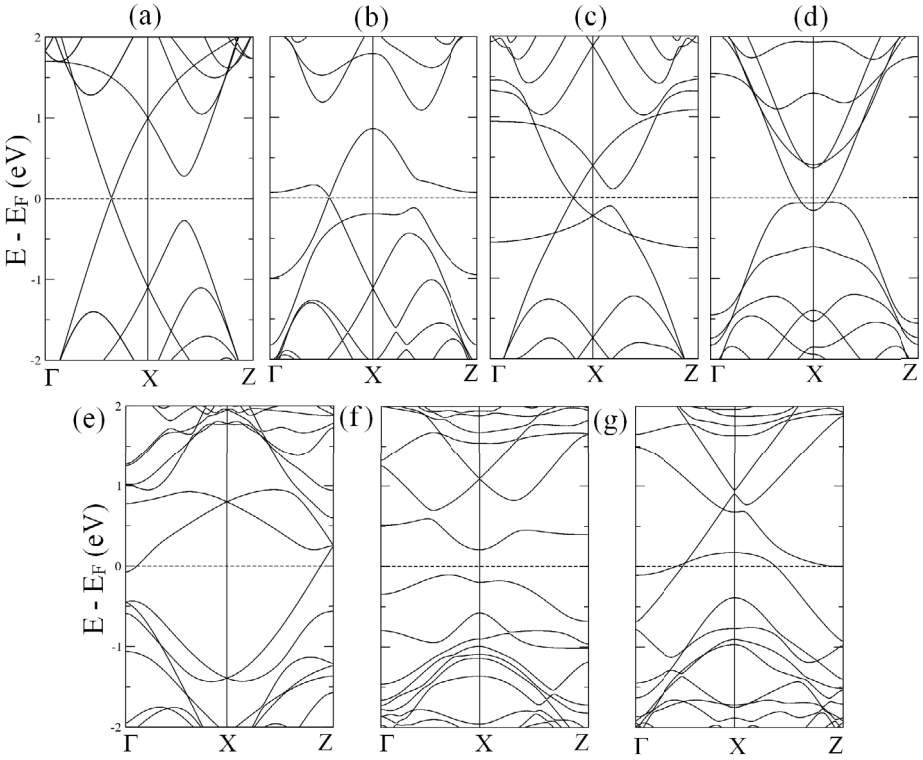

Fig. 3. Graphene band structures: (a) Pristine and having line defects composed by: (b) two pentagonal and one octagonal ring (558-LD), (c) tetragonal rings (4-LD), (d) tetradecanal rings (14-LD), (e) one tetragonal and one octagonal ring (48-LD). At (f) and (g) we have the punctual defects composed by two pentagons separated by one octagon in two different arrangements (585-PD_1 and 585-PD_2, respectively).

these σ states introduces sufficient electronic distortion to produce the imbalance in the π states. This strongly modifies the graphene electronic structure, which now presents a metallic character with two Dirac-like points in the valence band next to the X point (see Fig. 3d). Due to the metallic character a non null DOS with one peak can be seen at the Fermi level (see Fig. 4d). Dislocations in different directions introduces, in a 48-LD graphene sheet, sp^2-like hybridization and the sublattice symmetry breaking generates a drastically modified band structure as can be seen in Figure 3e, where we can clearly perceive the absence of the Dirac point and some bands crossing the Fermi level at the Γ and Z points, which gives the system a metallic character, as can be seen at the DOS at Figure 4e.

A single divacancy in graphene sheet results in the formation of a rearranged planar structure that encloses a central octagon and two opposing pentagonal rings, with sp^2 hybridization and the saturation of all dangling bonds. At Figure 3f we have the 585-PD_1 band structure showing the opening of a band gap of ≈0.27 eV. Ugeda and co-workers showed that the presence of this PD induces a dispersionless states next to the Fermi level with the opening of a band gap [33]. A null DOS at the Fermi level and peaks in the regions where there are dispersionless states are observed, as can be seen at Figure 4f.

Finally, we have the band structure of the system labeled 585-PD_2 at Figure 3g showing the Dirac point at the conduction band and two states clearly crossing the Fermi level and giving the system a metallic character that can be also seen at Figure 4g. We can see that the rotation of the 585-PD_1 in graphene can change states near the Fermi level. Hence, the inclusion of different defects at the perfect hexagonal lattice of graphene systems breaks the translational symmetry of the crystal, leading to profound changes in the low-energy electronic bands. In this manner, the controlled growth of graphene sheets, containing such defects can be a way to adjust their electronic properties going from semimetallic to metallic or semicondutor. Also, a simple alteration in the orientation of a single defect, like the 585-PD, can offer a possibility to change and adjust the properties of a given system.

3.1.2 Structural and magnetic properties

In this section, we perform a comparative analysis of formation energy and the magnetic moment by supercell (μ) of all studied graphene structures in order to see the energetic cost of a given defect and whether or not it makes the system to become magnetic, as can be seen at Table 1.

Our results are in accordance with the experimental observations, as can be seen in the following. At Table 1 it can be noticed that the 558-LD, 585-PD_1 and 585-PD_2, the experimentally observed systems [28,29,33,44], are the most stable defects. Those are followed by the 48-LD and

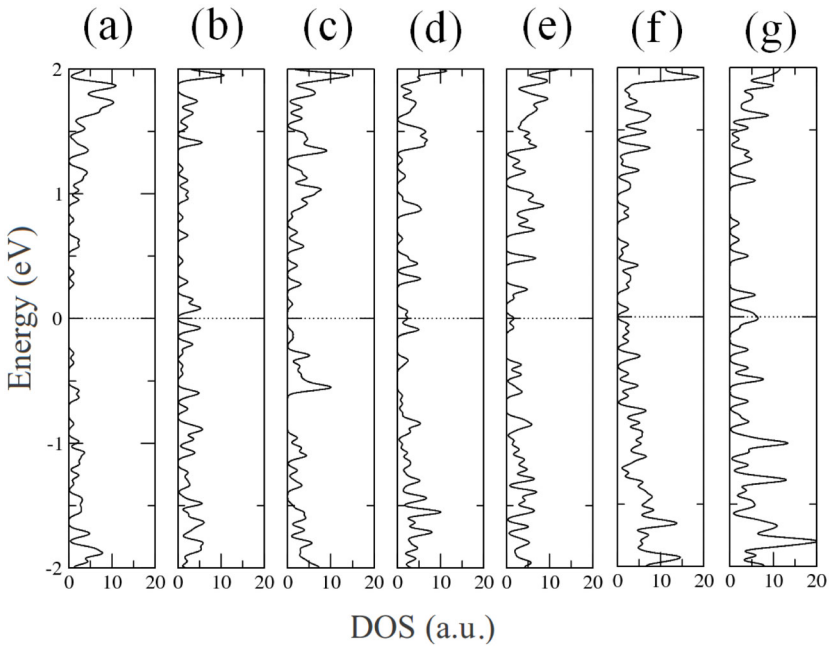

Fig. 4. Densities of states for the studied graphene systems: (a) Pristine and having line defects composed by: (b) two pentagonal and one octagonal ring (558-LD), (c) tetragonal rings (4-LD), (d) tetradecanal rings (14-LD), (e) one tetragonal and one octagonal ring (48-LD). At (f) and (g) we have the punctual defects composed by two pentagons separated by one octagon in two different arrangements (585-PD_1 and 585-PD_2, respectively).

Table 1. Formation energy (E_{for}) and the magnetic moment by supercell (μ) for the studied graphene systems.

Defect type	E_{for} (eV)	μ (μ_B)
No defect	0.00	0.00
558-LD	0.05	0.00
4-LD	0.18	0.00
14-LD	0.24	0.00
48-LD	0.17	0.00
585-PD_1	0.08	0.00
585-PD_2	0.14	0.00

4-LD, in this order. It is interesting to notice that the existence of the 4-LD system was predicted by Li et al. [30], while our results indicate an energetic advantage for the 48-LD. Finally, we can see that a simple rearrangement greatly alters the formation energy of a given graphene layer when we compare two systems with the same type of defects arranged in two different ways. This is the case of 558-LD (E_{for} = 0.05 eV) and 14-LD (E_{for} = 0.24 eV). At Figure 5 we have two different reconstruction processes of a line of divacancy at graphene. Removing the carbon dimers (inclined in relation to the zigzag orientation) results in an alternated series of one octagon plus two pentagons and the generation of a 558-LD structure (Fig. 5a). When this happens there are two atoms with only two σ bonds in the defect which facilitates the reconstruction process. On the other hand, if we remove carbon dimers oriented perpendicularly to the zigzag chains (Fig. 5b) is intuitively expected that, after geometrical relaxation, the structure would be composed of two pentagons separated by an octagon. However, what happens, due to the existence of four atoms with double bonds in the defect, is a different reconstruction process and the generation of a 14-LD structure (Fig. 5b).

At Figure 6 we have the geometry of defective graphene layers after relaxation, including bond angles and length. At Figure 6a, we notice that the introduction of a 558-LD does not drastically changes the C-C bond length (1.44 Å, for a regular graphene sheet). However, the bond angles suffer major variation when compared with the 120° of a perfect graphene hexagon. An interesting behaviour can be seen at Figure 6b, where we have two different views of a graphene layer containing a 4-LD: we have a distortion of the layer and two lines of atoms moved off the plane in opposite directions. This happens due to the type of chemical bonds presented by the C atoms at the central line defect: since each atom is four-coordinated, they present a sp^3 like hybridization and the bond angles at the central line vary from ≈60° to 71° after relaxation. Comparatively, the measured C-C bond distance after geometric optimization is 1.58 Å, similar to the one at diamond (1.58 Å). The divacancy line at Figure 6c increases the bond length of C atoms localized close to the defect center and decreases the bond length of atoms localized away of it. For the case of 48-LD system (Fig. 6d), the tetragonal ring presents two different bond lengths (1.38 and 1.50 Å) and the octagon presents different bond lengths and angles if compared to the one at Figure 6a, with higher values at the center and lower at the termination. At Figure 6e we have a punctual defect created from a divacancy with the pentagons presenting similar shape and bond angles which are very similar to those at Figure 6a, the exception being the octagonal ring bonds which are larger. Finally, we have the

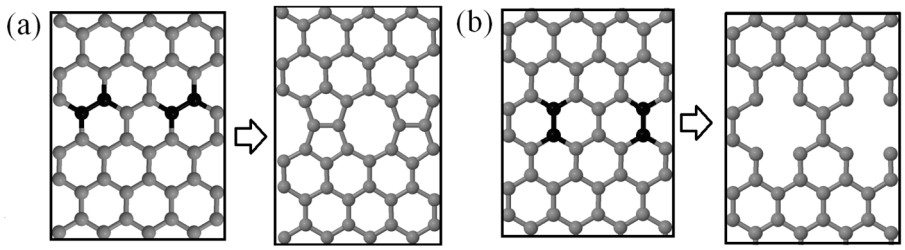

Fig. 5. Pictorial scheme for two different types of line defects formed starting from divacancies in a graphene layer. At (a) we have the formation of a line defect composed by two pentagonal rings (joined together by their bottom) and adjacent to one octagonal ring (558-LD). At (b) we have a line defects composed by tetradecanal rings (14-LD). The black spheres represent the removed atoms, which generate the divancancy.

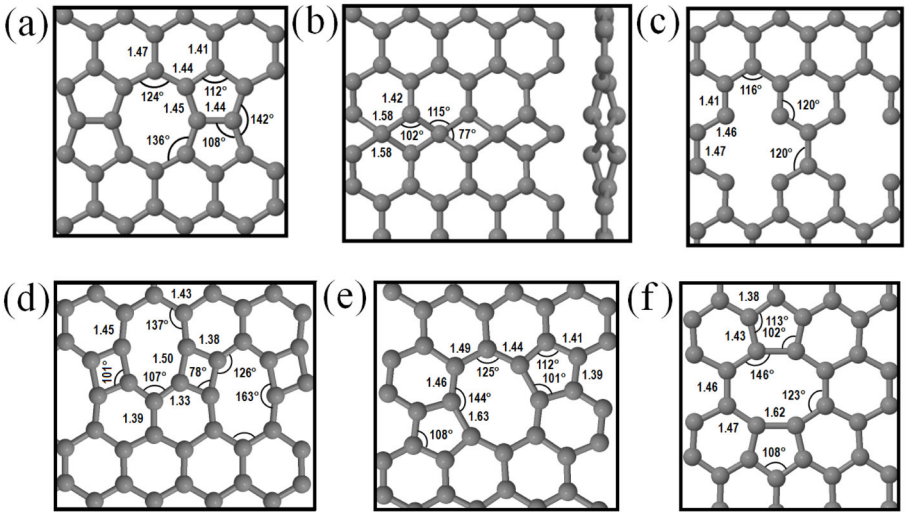

Fig. 6. Pictorial scheme for the studied graphene systems presenting line defects ((a) 558-LD, (b) 4-LD, (c) 14-LD, and (d) 48-LD) and punctual defects ((e) 585-PD_1 and (f) 585-PD_2) after geometric optimization. Some bond lengths (in Å) and angles are shown.

structure of 585-PD_2 (Fig. 6f), which is very similar to the previous one. Considering the magnetic properties of these defective graphene layers, it is valid to notice that none show any magnetization.

3.2 Graphene nanoribbons

3.2.1 Electronic properties

We have also investigated the modifications caused at the electronic properties of ZGNRs due to the inclusion of line defects and punctual defects. At Figure 7 we can see the band structures of these systems.

The band structure of a pristine 10-ZGNR, as can be seen at Figure 7a, presents the remarkable characteristic of having part of the higher state at the valence band and part of the lower state of conduction band degenerated at the Fermi level. For these states opposite directions linear dispersions can be also seen. The states at this region arise due to ZGNR edge states and, as a result, a pronounced peak is observed at the DOS shown at Figure 8a [12]. The inclusion of a 558-LD at the pristine 10-ZGNR introduces two new states, one above and one below the Fermi level (see Fig. 7b). As a result, we have a more pronounced peak at the Fermi level at the DOS and a smaller peak just below E_f (Fig. 8b). Furthermore, there was a state split at the conduction band. A similar result was also seen for the graphene with the same line defect as can be seen at Figures 3b and 4b. The incorporation, at the pristine 10-ZGNR, of a 4-LD introduces two states at ≈1.0 eV and ≈−0.5 eV (Fig. 7c). Also, the degeneracy is increased at E_f and, as a result, we have the high density of states observed around E_f at Figure 8c and two peaks in the region. These two states were also observed at the graphene containing the same defect as can be seen at Figure 3c. Therefore, the inclusion of 558- and 4-LD introduces close to the Fermi level states in graphene and ZGNR.

The imbalance between the σ and π states introduces sufficient electronic distortion to produce drastic alteration of the band structure of a pristine 10-ZGNR when we insert a 14-LD as shown at Figure 7d, which shows two highly delocalized states crossing E_f, the absence of states in the valence band and degenerated states at E_f. These results are corroborated by the DOS shown at Figure 8d.

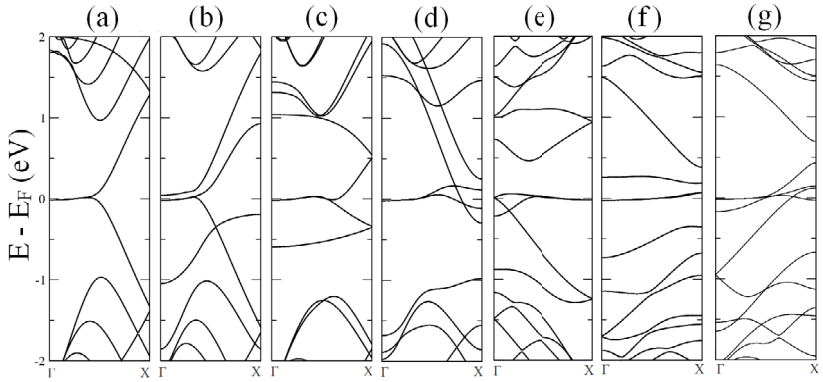

Fig. 7. Band structures for the studied zigzag graphene nanoribbons: (a) Pristine 10-ZGNR and having line defects composed by: (b) two pentagonal and one octagonal ring (558-LD-ZGNR), (c) tetragonal rings (4-LD-ZGNR), (d) tetradecanal rings (14-LD-ZGNR), (e) one tetragonal and one octagonal ring (48-LD-ZGNR). At (f) and (g) we have the punctual defects composed by two pentagons separated by one octagon in two different arrangements (585-PD_1-ZGNR and 585-PD_2-ZGNR, respectively).

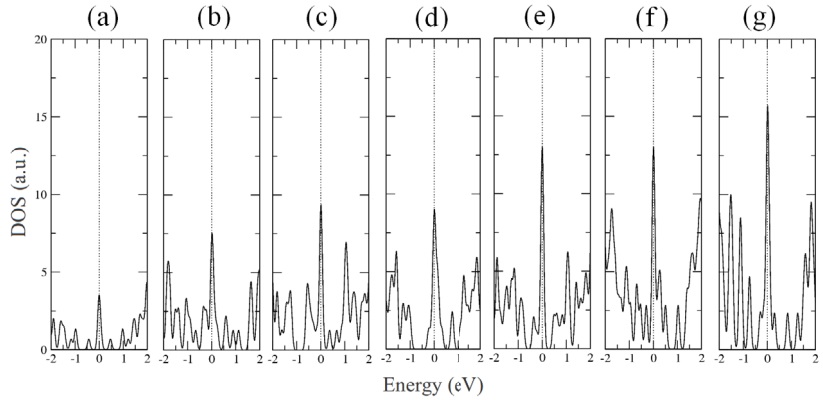

Fig. 8. Densities of states calculated for the studied zigzag graphene nanoribbons: (a) Pristine 10-ZGNR and having line defects composed by: (b) two pentagonal and one octagonal ring (558-LD-ZGNR), (c) tetragonal rings (4-LD-ZGNR), (d) tetradecanal rings (14-LD-ZGNR), (e) one tetragonal and one octagonal ring (48-LD-ZGNR). At (f) and (g) we have the punctual defects composed by two pentagons separated by one octagon in two different arrangements (585-PD_1-ZGNR and 585-PD_2-ZGNR, respectively).

A 48-LD breaks the sublattice symmetry generating a degenerated states along the E_f and a highly delocalized state at the valence band (Fig. 7e). The density of states, for this system, is shown at Figure 8e, where we can see a narrow and large peak at E_f. At Figure 7f it can be seen that the 585-PD_1 introduces two new and degenerated states along the Fermi level and another at the conduction band and also, a large peak is observed around E_f at the DOS (Fig. 8f). These dispersionless states next the Fermi level are also observed at the graphene containing the same defect as can be seen at Figure 3f. Finally, Figure 7g shows that the band structure of 585-PD_2 presents three degenerated and flat states at the Fermi level region with some highly delocalized levels crossing it. As a result, a large peak is observed at the E_f region at the DOS shown at Figure 8g. It can be seen that the rotation of 585-PD or the creation of divacancies on different lattice points in the lattice, in 10-ZGNRs, can change the states near the Fermi level.

As a general trend, it is observed that the inclusion of line and punctual defects in ZGNRs causes great variations at the electronic structure of these systems, in a similar way that was observed for graphene. However, for the case of ZGNRs the edge effects combined with states which arise due to the defects inclusion [45], a large number of states is observed. Also, higher values for the DOS at the Fermi level are observed for the ribbons if compared to the graphene systems. In addition, Figure 9 shows that the charge density is localized mainly at the edges, as expected.

The energy bands states of majority and minority spin are non degenerate for all ZGNRs and it is seen that all the majority states are crossing the Fermi level. This phenomenon implies the intense spin polarization and metallic behaviour with the exception of 585-LD_1-ZGNR, in which there is an energy gap between the valence and the conduction bands.

3.2.2 Structural and magnetic properties

We have related the calculated formation energies with the magnetic moment of the studied systems in order to

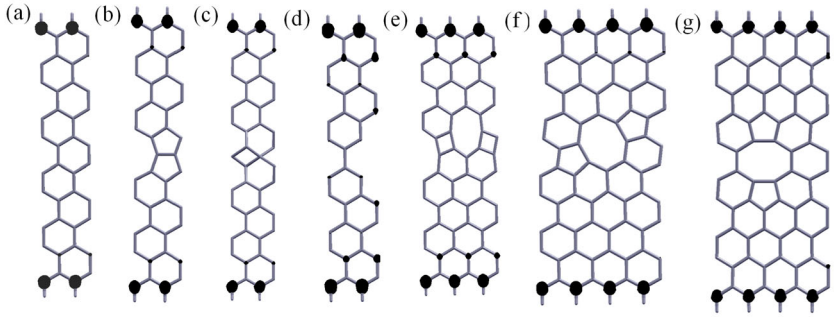

Fig. 9. Charge densities for the studied zigzag graphene nanoribbons: (a) Pristine 10-ZGNR, with line defects (b) 558-LD-ZGNR, (c) 4-LD-ZGNR, (d) 14-LD-ZGNR, (e) 48-LD-ZGNR, and with punctual defects (f) 585-PD_1-ZGNR, and (g) 585-PD_2-ZGNR.

Table 2. Formation energy (E_{for}) and the magnetic moment by supercell (μ) for the studied zigzag graphene nanoribbons.

Nanoribbons	E_{for} (eV)	μ (μ_B)
10-ZGNR	0.00	1.0
558-LD-ZGNR	0.05	0.9
4-LD-ZGNR	0.17	1.3
14-LD-ZGNR	0.22	1.6
48-LD-ZGNR	0.16	2.0
585-PD_1-ZGNR	0.08	2.0
5852-PD_2-ZGNR	0.14	2.0

investigate the energy cost of a given defect and whether or not it alters the ribbons magnetic properties. At Table 2 we have the results for the formation energy (E_{for}) for all studied ZGNRs together with the magnetic moment by supercell (μ).

It can be noticed, at first, that the formation energy results are very similar to the ones observed for the defective graphene systems. However, the same is not true for the magnetic properties of the studied ZGNRs. First of all, during the ribbons creation process and before H passivation, we have the carbons at the edges presenting one less σ and one less π bonds than the C at the ribbon inner part. The passivation process regenerates the σ bond, however, the electrons at the p_z orbitals are free to recombine and present edge states with localized bands at the Fermi level. The calculated magnetic moment is shown at Table 2 and it can be seen that the higher μ values are the ones presented by the 48-LD-ZGNR, 585-PD_1, and 585-PD_2 systems and, amongst these, the defect presenting the lowest energy cost is the 585-PD_1.

As the last analysis, we calculate as the magnetic moment by supercell (μ) and formation energy (E_{for}) for the ZGNR without defects as a function of the number of zigzag chains (N_z) across the ribbons as can be seen at Figure 10. As we increase the ribbons width we have observed some kind of transition, indicating the switching of the magnetic coupling between opposite ribbon edges from the antiferromagnetic to the ferrimagnetic and ferromagnetic configurations. The results for formation energy show that it decreases with the increasing of width for $N_z > 2$.

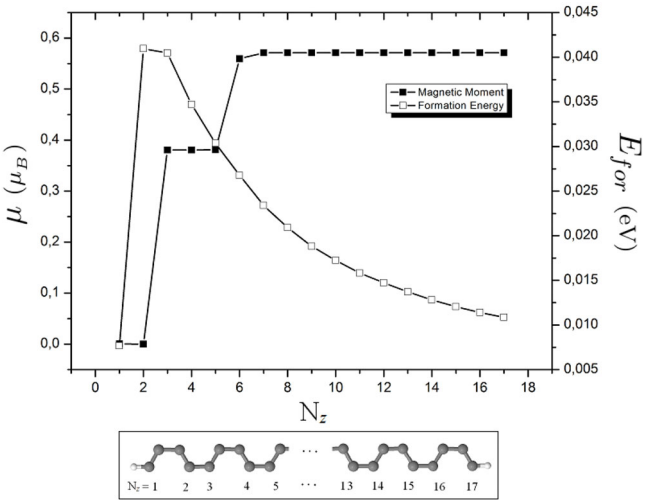

Fig. 10. Magnetic moment and formation energy for defect free zigzag graphene nanoribbons as a function of the number of zigzag chains across the ribbons for $N_z = (1–17)$.

4 Conclusions

In summary, through first-principles calculations, we have investigated the changes at the structural, energetic, electronic, and magnetic properties of graphene and ZGNRs due to the inclusion of several types of defects. It was seen that, depending on the type of defect, the graphene maintains its semimetallic character or becomes metallic or semiconductor. The inclusion of different defects at the perfect hexagonal lattice of graphene systems breaks the translational symmetry of the crystal, leading to profound changes in the low-energy electronic bands. In this manner, the controlled growth of such structures suggests a new way to tune the electronic properties of graphene, which are extremely important to promote possible applications in a wide variety of nanoelectronic devices.

At the ZGNRs, the inclusion of defects plays an important role in controlling the states at the Fermi level, which are manifested by pronounced peaks in the density of states. These pronounced peaks at the Fermi level are the result of edge effects combined with the states which arise due to the defects inclusion and are very important

for the observation of many strongly correlated phenomena such as ferromagnetism, superconductivity and fractional quantum Hall effect in ZGNRs.

The defective ZGNRs structures show magnetic moment by supercell up to $2.0\mu_B$. For the defect free ZGNRs it was seen that the ribbon width plays an important role at both the formation energy and magnetic coupling between opposite edges, going from antiferromagnetic, to ferrimagnetic and ferromagnetic. Such behaviour can have important implications at the spintronic.

We would like to thank the financial support given by the Brazilian Agencies FAPESB, CNPq, INCT – Nanomateriais de Carbono, and Capes/Nanobiotec.

References

1. K.S. Novoselov, A.K. Geim, S.V. Morozov, D. Jiang, Y. Zhang, S.V. Dubonos, I.V. Grigorieva, A.A. Firsov, Science **306**, 666 (2004)
2. C. Lee, X. Wei, J.W. Kysar, J. Hone, Science **321**, 385 (2008)
3. R.R. Nair, P. Blake, A.N. Grigorenko, K.S. Novoselov, T.J. Booth, T. Stauber, N.M.R. Peres, A.K. Geim, Science **320**, 1308 (2008)
4. X. Ma, H. Zhang, Nanoscale Res. Lett. **8**, 440 (2013)
5. A.H. Castro Neto, F. Guinea, N.M.R. Peres, K.S. Novoselov, A.K. Geim, Rev. Mod. Phys. **81**, 109 (2009)
6. A.K. Geim, K.S. Novoselov, Nat. Mater. **6**, 183 (2007)
7. L.M. Viculis, J.J. Mack, R.B. Kaner, Science **299**, 1361 (2003)
8. K.S. Novoselov, D. Jiang, F. Schedin, T.J. Booth, V.V. Khotkevich, S.V. Morozov, A.K. Geim, Proc. Natl. Acad. Sci. USA **102**, 10451 (2005)
9. A.N. Obraztsov, E.A. Obraztsova, A.V. Tyurnina, A.A. Zolotukhin, Carbon **45**, 2017 (2007)
10. L. Pisani, J.A. Chan, B. Montanari, N.M. Harrison, Phys. Rev. B **75**, 064418 (2007)
11. Y.-W. Son, M.L. Cohen, S.G. Louie, Phys. Rev. Lett. **97**, 216803 (2007)
12. K. Nakada, M. Fujita, G. Dresselhaus, M.S. Dresselhaus, Phys. Rev. B **54**, 17954 (1996)
13. W.Y. Kim, K.S. Kim, Nat. Nanotechnol. **3**, 408 (2008)
14. F. Muñoz-Rojas, J. Fernández-Rossier, J.J. Palacios, Phys. Rev. Lett. **102**, 136810 (2009)
15. J. Baringhaus, M. Ruan, F. Edler, A. Tejeda, M. Sicot, A. Taleb-Ibrahimi, A.-P. Li, Z. Jiang, E.H. Conrad, C. Berger, C. Tegenkamp, W.A. de Heer, Nature **506**, 349 (2014)
16. L. Tapaszto, G. Dobrik, P. Lambin, L.P. Biro, Nat. Nanotech. **3**, 397 (2008)
17. G.Z. Magda, X. Jin, I. Hagymási, P. Vancsó, Z. Osváth, P. Nemes-Incze, C. Hwang, L.P. Biró, L. Tapasztó, Nature **514**, 608 (2014)
18. J. Cai, P. Ruffieux, R. Jaafar, M. Bieri, T. Braun, S. Blankenburg, M. Muoth, A.P. Seitsonen, M. Saleh, X. Feng, K. Müllen, R. Fasel, Nature **466**, 470 (2010)
19. T.H. Vo, M. Shekhirev, D.A. Kunkel, M.D. Morton, E. Berglund, L. Kong, P.M. Wilson, P.A. Dowben, A. Enders, A. Sinitskii, Nat. Commun. **5**, 1 (2014)
20. L. Jiao, X. Wang, G. Diankov, H. Wang, H. Dai, Nat. Nanotechnol. **5**, 321 (2010)
21. J. Yuan, L.-P. Ma, S. Pei, J. Du, Y. Su, W. Ren, H.-M. Cheng, ACS Nano **7**, 4233 (2013)
22. Y.-H. Zhang, K.-G. Zhou, K.-F. Xie, J. Zeng, H.-L. Zhang, Y. Peng, Nanotechnol. **21**, 065201 (2010)
23. H. Hiura, Appl. Surf. Sci. **222**, 374 (2004)
24. B. Xu, J. Yin, Y.D. Xia, X.G. Wan, K. Jiang, Z.G. Liu, Appl. Phys. Lett. **96**, 163102 (2010)
25. D. Ghosh, P. Parida, S.K. Pati, J. Mater. Chem. C **2**, 392 (2014)
26. M. Pelc, L. Chico, A. Ayuela, W. Jaskólski, Phys. Rev. B **87**, 165427 (2013)
27. Q.Q. Dai, Y.F. Zhu, Q. Jiang, J. Phys. Chem. C **117**, 4791 (2013)
28. J. Lahiri, Y. Lin, P. Bozkurt, I.I. Oleynik, M. Batzill, Nat. Nanotechnol. **5**, 326 (2010)
29. J.-H. Chen, G. Autís, N. Alem, F. Gargiulo, A. Gautam, M. Linck, C. Kisielowski, O.V. Yazyev, S.G. Louie, A. Zettl, Phys. Rev. B **89**, 121407(R) (2014)
30. Y. Li, R.-Q. Zhang, Z. Lin, M.A.V. Hove, Nanoscale **4**, 2580 (2012)
31. W. Zhou, X. Zou, S. Najmaei, Z. Liu, Y. Shi, J. Kong, J. Lou, P.M. Ajayan, B.I. Yakobson, J.-C. Idrobo, Nano Lett. **13**, 2615 (2013)
32. A.R. Botello-Méndez, X. Declerck, M. Terrones, H. Terronesa, J.-C. Charliera, Nanoscale **3**, 2868 (2011)
33. M.M. Ugeda, I. Brihuega, F. Hiebel, P. Mallet, J.-Y. Veuillen, J.M.G. Rodríguez, F. Ynduráin, Phys. Rev. B **85**, 121402(R) (2012)
34. Y. Liu, X. Zou, B.I. Yakobson, ACS Nano **6**, 7053 (2012)
35. D. Sanchez-Portal, P. Ordejon, E. Artacho, J.M. Soler, Int. J. Quantum Chem. **65**, 435 (1997)
36. J.M. Soler, E. Artacho, J.D. Gale, A. Garcia, J. Junquera, P. Ordejon, D. Sanchez-Portal, J. Phys.: Condens. Matter **14**, 2745 (2002)
37. P. Hohenberg, W. Kohn, Phys. Rev. B **136**, B864 (1964)
38. W. Kohn, L. Sham, Phys. Rev. Lett. **140**, A1133 (1965)
39. J.P. Perdew, S. Burke, M. Ernzerhof, Phys. Rev. Lett. **77**, 3865 (1996)
40. N. Troullier, J. Martins, Phys. Rev. B **43**, 1993 (1991)
41. L. Kleinman, M. Bylander, Phys. Rev. Lett. **48**, 1425 (1982)
42. S.S. Alexandre, H. Chacham, R.W. Nunes, Phys. Rev. B **63**, 045402 (2001)
43. S. Azevedo, M.S. Mazzoni, R.W. Nunes, H. Chacham, Phys. Rev. B **70**, 205412 (2004)
44. J. Kotakoski, A.V. Krasheninnikov, U. Kaiser, J.C. Meyer, Phys. Rev. Lett. **106**, 105505 (2011)
45. L. Feng, X. Lin, L. Meng, J.-C. Nie, J. Ni, L. He, Appl. Phys. Lett. **101**, 113113 (2012)